Kovove Mater. 61 2023 69–80
DOI: 10.31577/km.2023.2.69

Effects of hot deformation on microstructure evolution, hardness, and intergranular corrosion of 7085 aluminum alloy sheets

Jiangjing Wu, Xizhou Kai, Chuang Guan, Rui Cao, Yutao Zhao*

School of Material Science and Engineering, Jiangsu University, Zhenjiang Jiangsu 212013, P. R. China

Received 31 October 2022, received in revised form 1 February 2022, accepted 13 February 2023

Abstract

In this work, slabs of 7085 aluminum alloy were fabricated by electromagnetic stirring and solidifying with copper mold and suffered hot plastic deformation. The straight hot rolling process was used when the slabs were preheated to 420 °C for 1 h. The thicknesses of 1-, 2-, and 3-mm sheets correspond to the thickness reduction rate of 92, 83, and 75 % of original rectangular slabs. The microstructure results show that hot rolling deformation crushes the remanent phases into small sizes, leads particles into homogeneous distribution, and changes the dendritic grain into a fiber structure. The recrystallization rate decreases with the final sheet thickness increase after heat treatment. The recrystallization is strictly restricted when the thickness reduction rate approaches 92 %. EBSD results provide a unique perspective to view grain and dislocation evolution and texture change in different tempers of sheets. The hardness and intergranular corrosion (IGC) performance show that hardness is reduced while the corrosion depth is aggravated by the rise of sheet thickness. The maximum hardness is 86.75 HRB, and the minimum corrosion depth is only 9.17 μm in the 1-mm sheet. The effects of grain boundary precipitates (GBPs), recrystallization, and precipitate-free zone (PFZ) on hardness and IGC were studied.

K e y w o r d s: grain boundaries, recrystallization, dislocation, hardness, intergranular corrosion (IGC)

1. Introduction

Al-Zn-Mg-Cu alloy has high strength and excellent toughness in industrial applications such as aviation, mold, and transportation [1–4]. Due to end-user requirements, aluminum alloy with all-around performance has been an urgent need recently. Nowadays, with energy-saving and emission-reduction demands, the selection of lightweight and high-strength aluminum sheets is becoming a tendency in the auto industry. 5xxx and 6xxx aluminum alloy sheets are widely employed in the inner or outer door panels and aluminum body sheets (ABS) [5–7]. However, new types of aluminum sheets are badly needed besides the current aluminum sheets due to application demands for other steel replacements. Moreover, with further weight loss requirements in the new energy auto industry, the tendency to develop high-performance aluminum sheets is becoming an urgent need. Hence, it is significant to study new aluminum sheets to fulfil automotive applications.

Recently 7xxx aluminum alloy has been mainly used as structural components in the automotive field. Extruded 7050 and 7075 aluminum parts in A-pillar or B-pillar are typical applications in new-generation autos [8–10]. Though the sheet product application for 7xxx alloy in auto is limited due to the difficulties in room temperature formability compared with that of 5xxx or 6xxx sheets, it is still worth to further studying the sheets for 7xxx alloy if the hot forming technology is gradually accepted by the manufacturers [11].

As known to us, 7085 alloy is a highly high-strength alloy with a certain toughness, and its main application is structural parts for aviation and molding for cavities [12, 13]. To expand its application scope, severe plastic deformation (SPD) techniques such as hot

*Corresponding author: e-mail address: zhaoyt@ujs.edu.cn

rolling, cryo rolling, and hot forging have been used to improve mechanical properties [14, 15]. These plastic deformations result in microstructure homogenization along the deformation direction and high dislocation density, which can become the nucleation sites for the precipitate. After suitable heat treatment, the stable precipitates with proper morphology from the matrix are the key factors for strengthening. Due to the high zinc content in 7085 aluminum alloy, $\eta(MgZn_2)$ is the grain boundary precipitate [16, 17]. The distribution and morphology of the η phase are sensitive to IGC [18–21]. Thus, it is necessary to evaluate the effects of precipitates after plastic deformation and heat treatment on mechanical properties and corrosion resistance.

Considering all these factors, the relationship between plastic deformation rate and material performance needs to be built. 7085 aluminum alloy was selected as a matrix for the sheet. The microstructure was modulated by hot deformation and heat treatment to investigate hardness and IGC. The aim of this paper is to provide an essential performance reference for high-performance 7085 aluminum sheets.

2. Experimental procedure

2.1. Fabrication of 7085 aluminum alloy sheets

The raw materials in the experiment are pure aluminum (> 99.9 %), pure zinc (> 99.9 %), pure magnesium (> 99.9 %), copper wire (> 99.9 %), Al-5%Zr hardener, and Al-6%Ti hardener. The pure elements were melted in a graphite crucible with a high-frequency induction heating furnace. The melt was kept at 750 ± 10 ℃ for 10 min and was stirred by 10 Hz electromagnetic stirring alternatingly for 5 min and mechanical stirring for 1 min. Then the melt was degassed and purified with C_2Cl_6. Finally, the melt was poured into a pre-heated (200 ℃) copper mold at 710 ± 10 ℃. The slabs were cut into rectangular specimens with 30 mm (TD, transverse direction) × 60 mm (RD, rolling direction) × 12 mm (ND, normal direction) and heated up to 470 ℃-10 h for homogenization to eliminate the local segregation, then the specimens were preheated to 420 ℃ with soaking for 1 h; finally, they were subjected to hot rolling to the thickness of

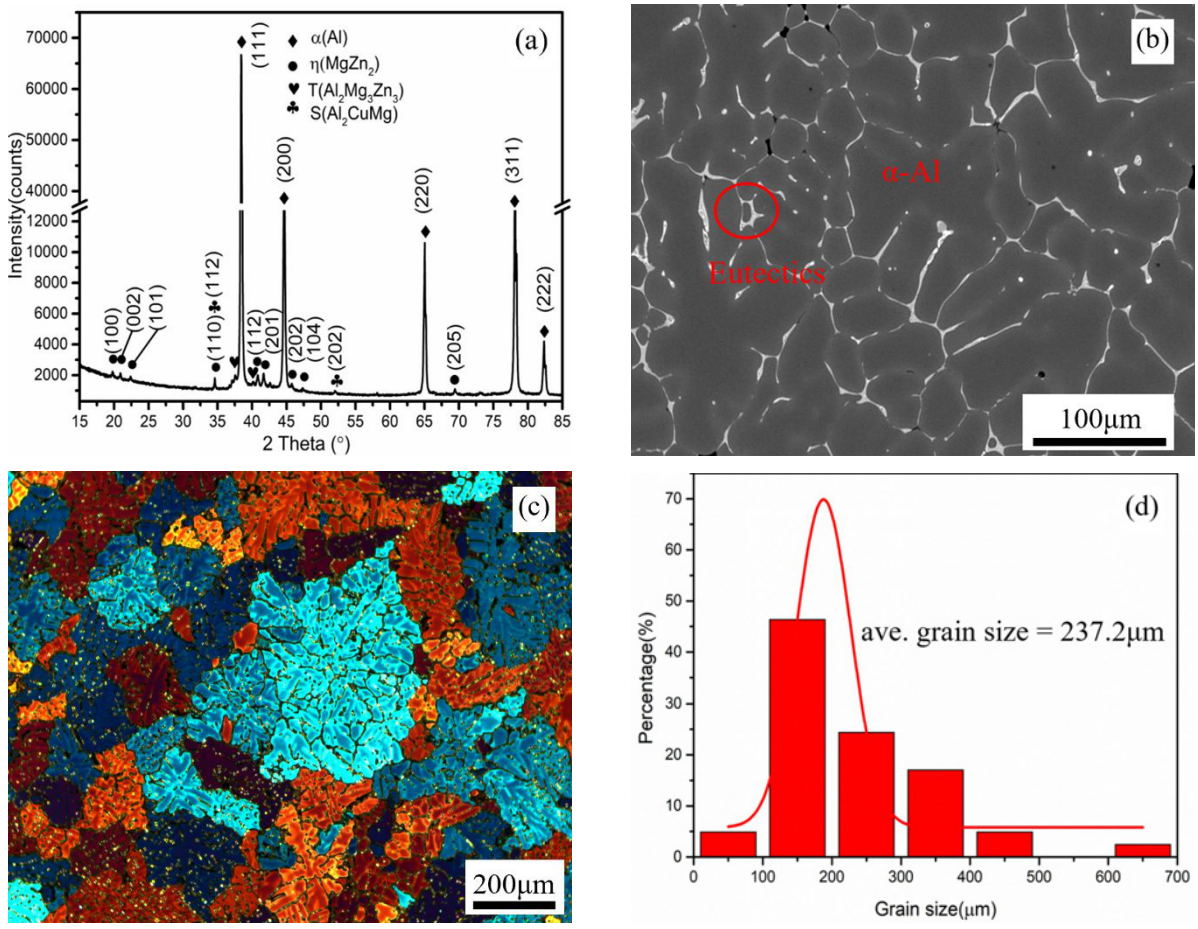

Fig. 1. X-ray diffraction patterns, microstructure, and grain structure of as-cast 7085 alloy: (a) X-ray diffraction patterns, (b), (c) as-cast microstructure and grain, and (d) the average grain size.

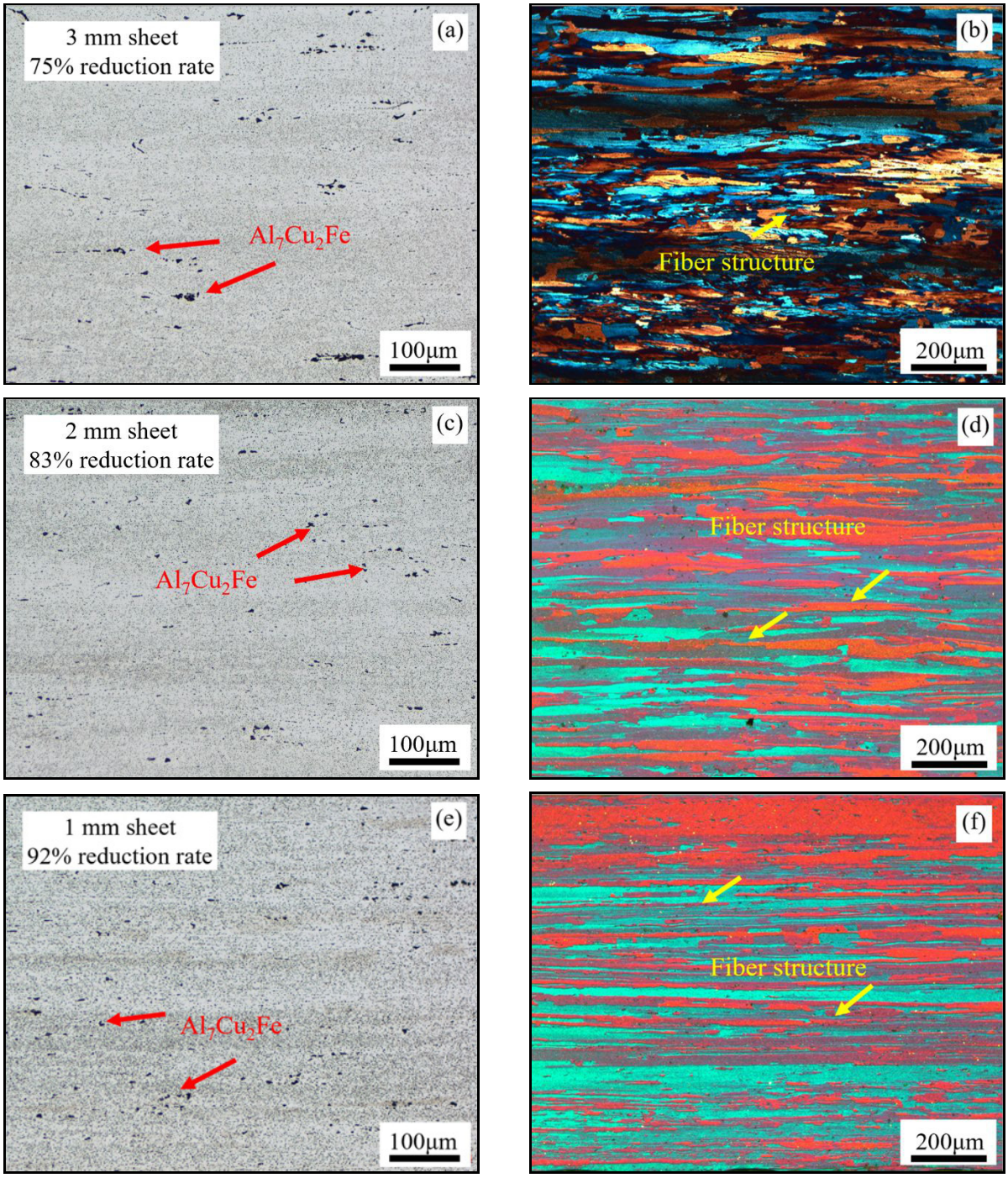

Fig. 2a–f. Microstructure and grain structure of 7085 sheets in different processes: (a), (c) and (e) as-rolled microstructure and (b), (d) and (f) grain of different thickness sheets.

1, 2, and 3 mm sheets. The rolling method is based on the continuous rolling process without heating up for each reduction step during rolling. The heat treatment process for sheets was 460 ℃-10 min for the solid solution and 120 ℃-5 h/160 ℃-10 h for artificial aging.

2.2. Characterization methods

The X-Ray Diffraction (XRD) and Inductively Coupled Plasma-Optical Emission Spectroscopy (ICP-OES) were applied to phase identification for the as-cast 7085 slabs. Optical microscope (OM) for microstructure and anodic lamination, scanning electron microscope (SEM) with electron backscattered diffraction (EBSD), and transmission electron microscope (TEM) were employed by Zeiss Image, FEI Nova Nano 450 instrument, FEI Talos F200X, respectively. The microstructure, grain structure, EBSD, and cor-

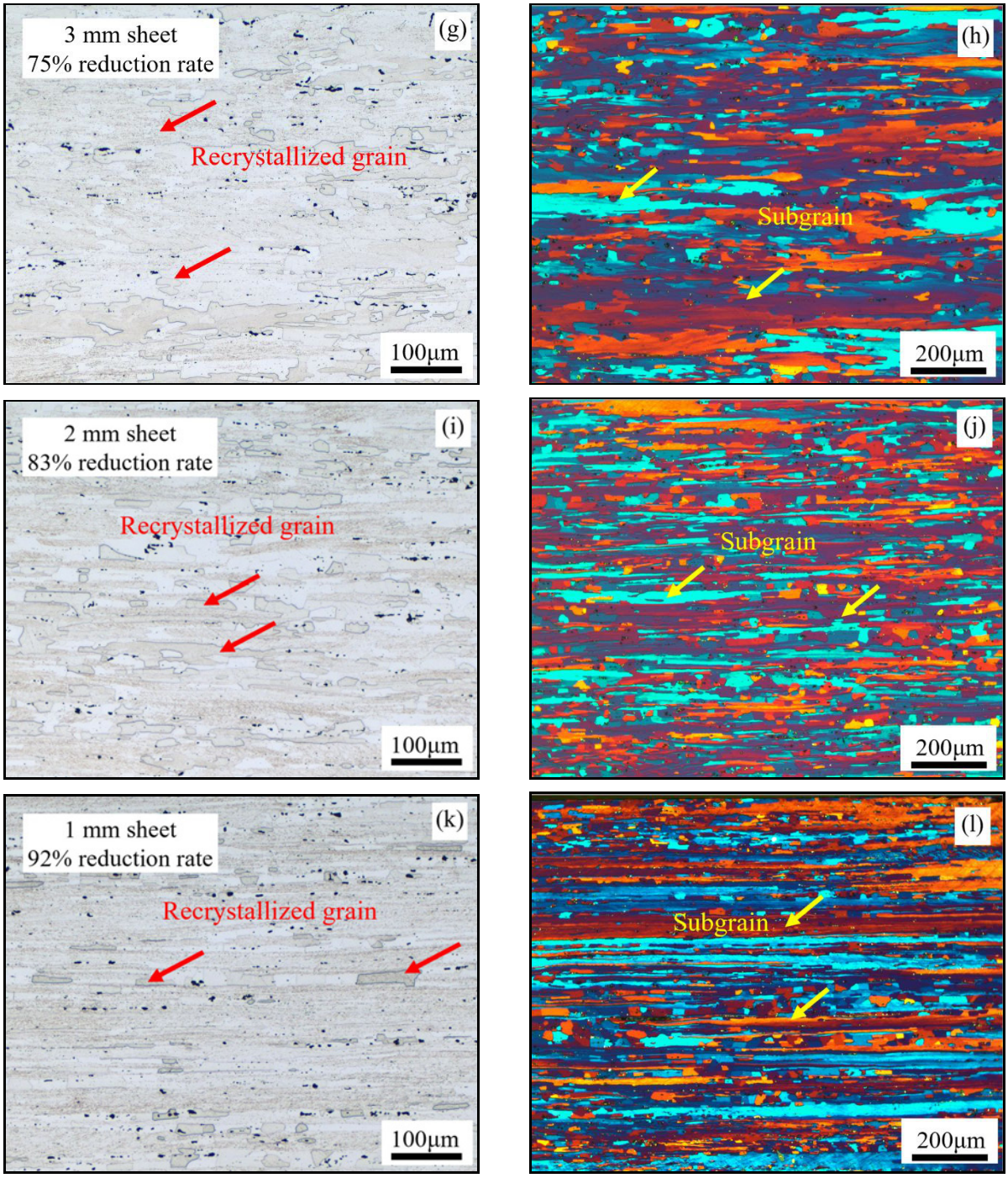

Fig. 2g–l. Microstructure and grain structure of 7085 sheets in different processes: (g), (i) and (k) microstructure and (h), (j) and (l) grain of different thickness sheets after heat treatment.

rosion depth were observed along the RD-ND plane, and the hardness test was conducted on the RD-TD plane.

3. Results and discussion

3.1. Chemical composition of 7085 alloy

The chemical composition of the 7085 aluminum alloy sheet by ICP-OES is shown in Table 1.

Table 1. Chemical composition of the 7085 aluminum alloy sheet (%, mass fraction)

Element	Zn	Mg	Cu	Fe	Si	Zr	Ti	Al
Content	7.57	2.06	1.57	0.08	0.03	0.13	0.03	Bal.

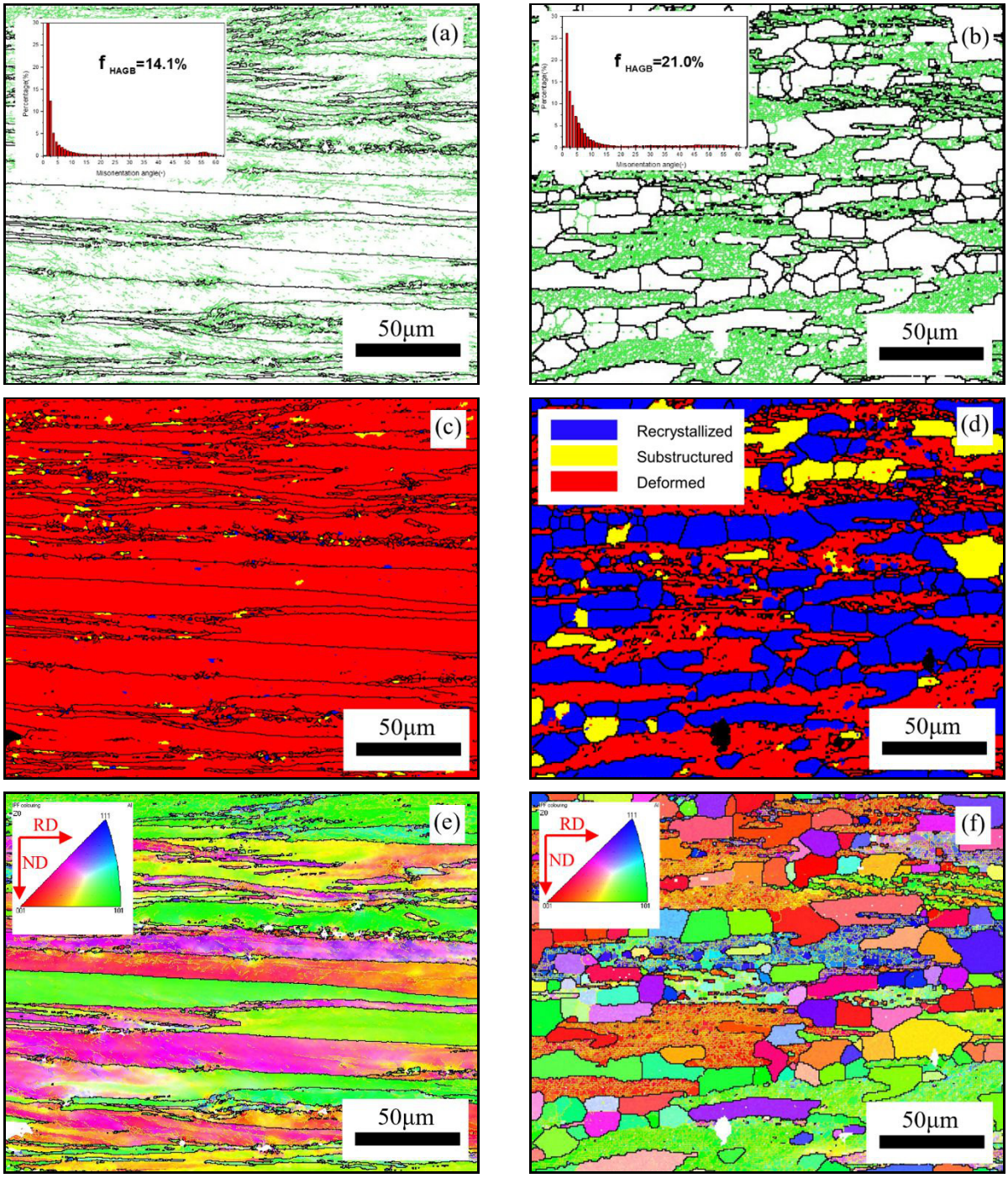

Fig. 3. EBSD maps of as-rolled and heat treated 7085 alloy with 2 mm thickness sheet: (a) and (b) grain boundary distrbution, (c) and (d) recrystallization distribution, (e) and (f) TD-IPF maps.

3.2. XRD analysis and microstructure evolution of 7085 alloy

XRD patterns of as-cast 7085 alloys with the constituent phases (α-Al, $\eta(MgZn_2)$, $S(Al_2CuMg)$, and $T(Al_2Mg_3Zn_2)$) are shown in Fig. 1a [1, 22]. Besides the strong peak associated with α-Al, the substrong peak is related to $\eta(MgZn_2)$. As shown in Fig. 1b, the typical solidification microstructure of as-cast 7085 alloys is α-Al and the second phases include η, S, and T along the grain boundary, which are shown in the eutectic morphology. Also, impurity phase such as Al_7Cu_2Fe from raw material and casting exists on the microstructure [23]. The grain structure of the casting alloy is shown in Fig. 1c, the dendritic growth in different size ranges exhibits the grain morphology results from a competitive growth relationship during solidifi-

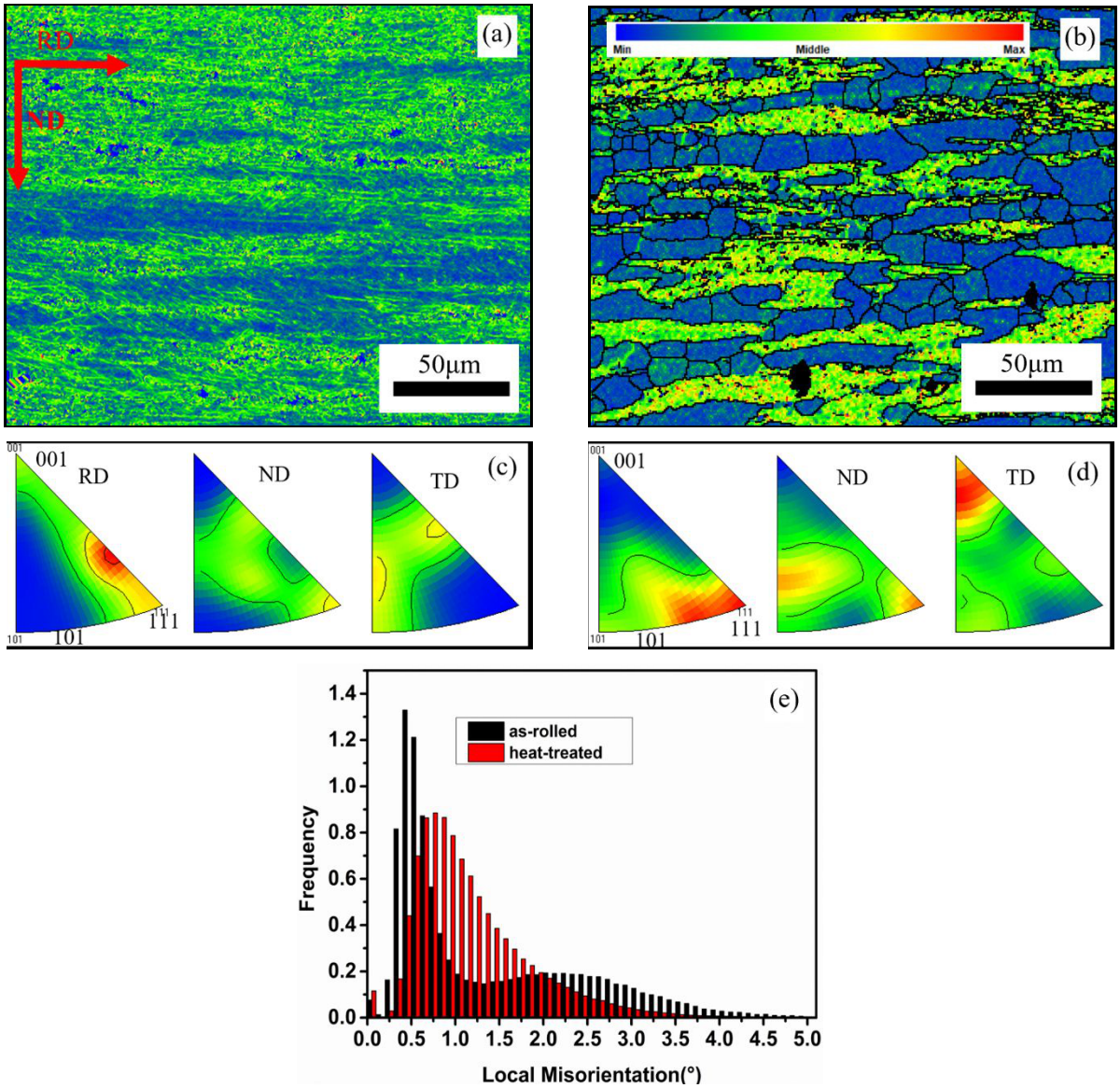

Fig. 4. Kernel average misorientation (KAM) maps and inverse pole figures (IPFs) of 2 mm thickness sheet: (a) and (b) KAM maps of specimens with as-rolled and heat-treated status, (c) and (d) IPFs of specimens with as-rolled and heat-treated status, (e) misorientation distribution of specimens with as-rolled and heat-treated status.

cation, and the average grain size is 237.2 μm in Fig. 1d.

The rolling structures of 7085 sheets with different thicknesses are shown in Figs. 2a,c,e and the second phases, especially Al_7Cu_2Fe, are gradually broken into small particles marked with red arrows along the rolling direction with hot deformation from 75 to 92 % reduction rate, and the Al_7Cu_2Fe phase becomes a highly tiny particle in the 1 mm sheet. Additionally, the grain morphology in Figs. 2b,d,f is changed from a dendritic structure (Fig. 1c) to an elongated grain structure marked with yellow arrows according to the corresponding reduction rate. A typical rolling structure with fiber features can be obtained when the reduction approaches 92 %. After heat treatment, the distribution of nano-size precipitates in Figs. 2g,i,k is gradually from inhomogeneous to homogeneous due to the grain layers narrowing along the ND direction. The grain structure tends to appear partial recrystallization with sub-grain in Figs. 2h,j,l, and large-scale recrystallized grains exist in the 3 mm sheet with a reduced rate of 75 %. Meanwhile, the recrystallization rate is decreased with the reduction of sheet thickness.

As shown in Fig. 3, EBSD maps provide details of grain structure evolution from an as-rolled to a heat-treated structure. Figures 3a,b show the grain boundary distribution of as-rolled and heat-treated sheets and the results exhibit that value of high-angle grain boundaries (HAGBs) in the black line reaches 14.1 % after rolling, and the value in heat-treated status is

21.0 %. From Fig. 3c, the volume fraction of recrystallized grain marked with blue color in as-rolled status is only 1.0 % with a very high-volume fraction of deformed structure, while the recrystallization rate is 43.4 % after heat treating in Fig. 3d. For the as-rolled sheet with 83 % thickness reduction, such hot deformation almost results in fiber structure along the rolling direction without any as-cast structure. As the degree of dynamic recrystallization (DRX) [24] is related to the proportion of HAGBs, and at the same time the low ratio of DRX results from only a very low proportion of HAGBs, the remaining HAGBs are attributed to hot plastic deformation in Figs. 3a,c.

RD and TD are marked in Figs. 3e,f. The grain colors combined with the Euler triangle legend reflect the preferred orientation of grains. [101] and [001] orientations are considered the main ones for the as-rolled structure in Fig. 3e. After heat treatment, the grain orientation of [111] appears beside the two preview orientations in Fig. 3f. The change of preferred grain orientation is mainly caused by recrystallization behavior. Plenty of dislocations are stored in the [111] orientation grains, and the driving force for recrystallization is relatively high; thus the [111] orientation grains are preferential recrystallization, and eventually, a large number of recrystallized grains nucleate and grow in the region [14].

The KAM is applied to describe the distribution of local dislocation density. As shown in Figs. 4b, the intensity of local dislocation density is partially decreased but remains a high dislocation density in the local zone after heat treatment.

Figures 4c,d manifest the texture change from the as-rolled to the heat-treated temper along three orientations. For RD orientation, the texture <111> // RD occurs both at as-rolled and heat-treated status, which is the same texture type for the two tempers. As found along ND orientation, there is no strong texture on the as-rolled specimen, while the texture <111> // ND gradually appears after heat treatment. The texture evolution along TD orientation is the appearance of the strong texture <001> // TD by solid solution and artificial aging, and this phenomenon confirms the increase of the local dislocation density in Fig. 4b. In the heat treatment process, the recrystallized grains with different orientations generate from the elongated structure, and these new equiaxed grains result in the texture change.

Figure 4e displays the misorientation distribution of specimens with as-rolled and heat-treated status. For as-rolled specimens, the low-angle grain boundaries (LAGBs) with misorientation angles below 2° take a large proportion, while the sub-grain boundaries with misorientation angles below 1° occupy a large percentage for heat-treated specimens. It indicates that smaller LAGBs or sub-grains tend to result in higher dislocation density in the local region. The

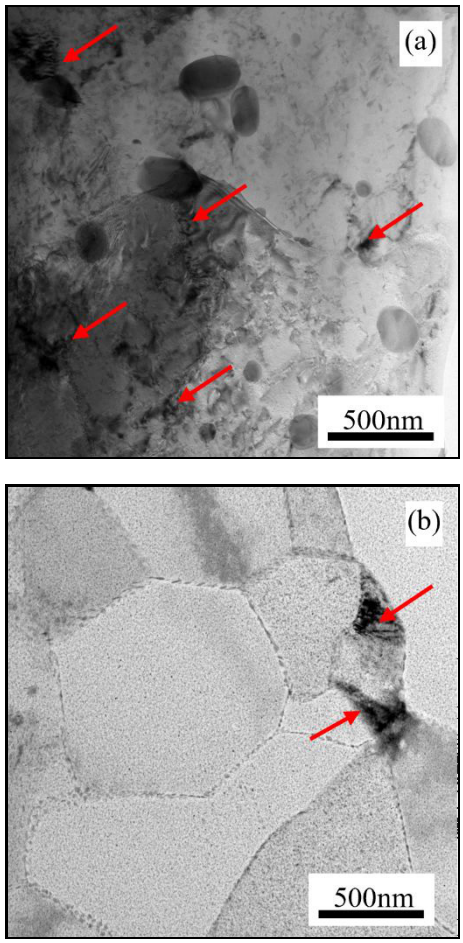

Fig. 5. TEM photos of dislocation evolution from different tempers: (a) as-rolled, (b) heat-treated.

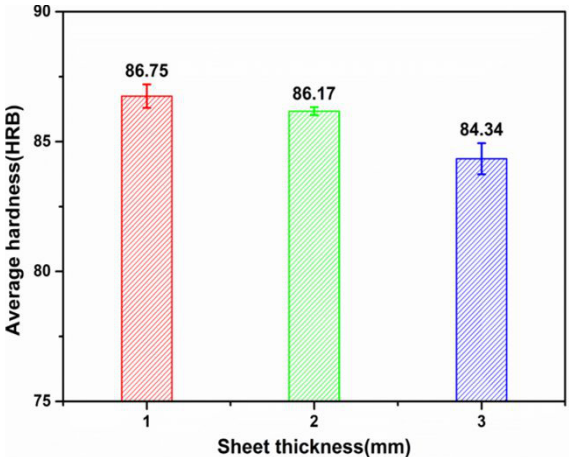

Fig. 6. Surface average hardness from different thickness sheets.

sub-grains on heat-treated specimens are mainly due to the nano-size spherical Al_3Zr precipitate which is coherent with the aluminum matrix [21]. The Al_3Zr

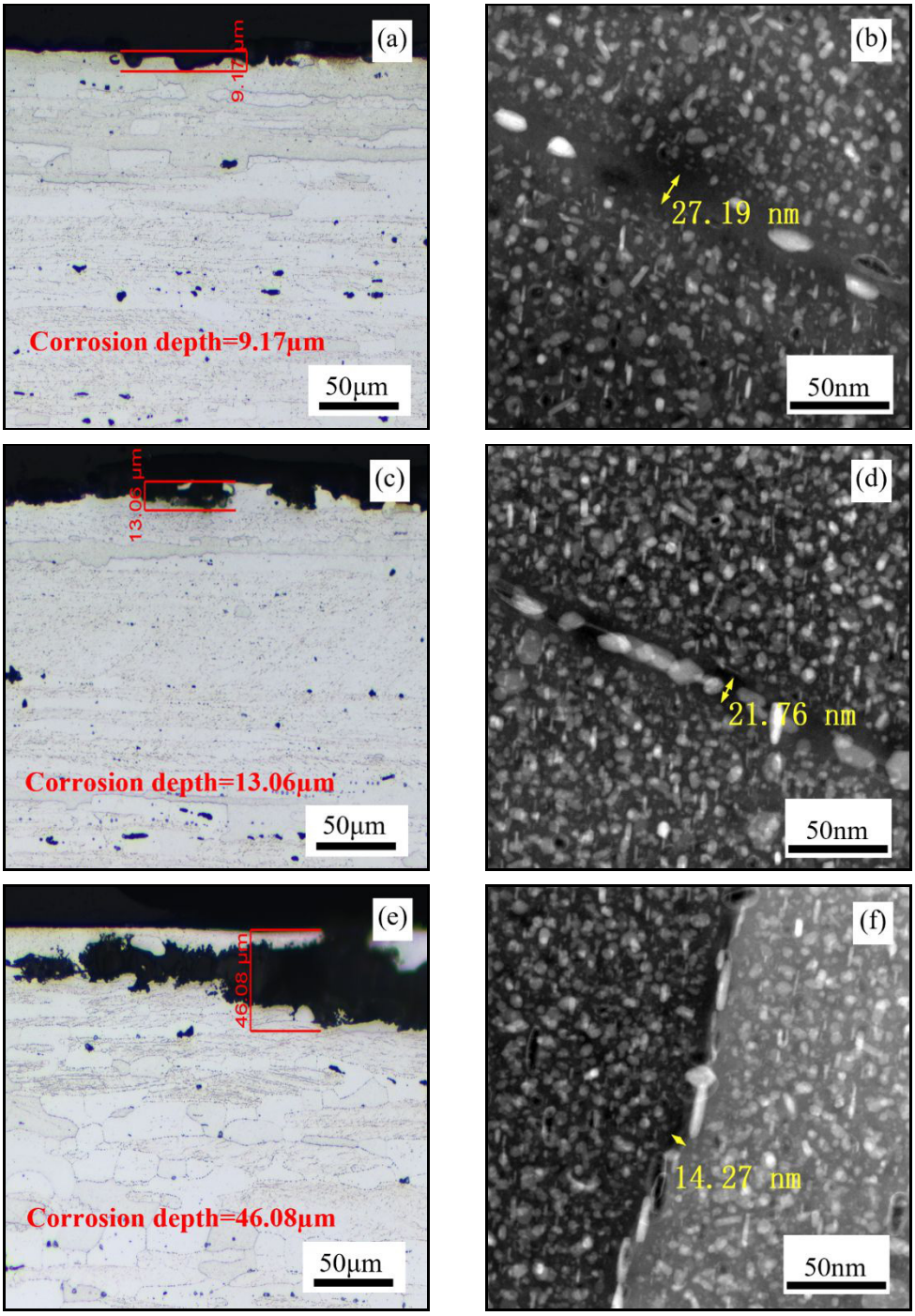

Fig. 7a–f. Corrosion depths and TEM images of precipitate on 1 mm, 2 mm and 3 mm thickness sheets and element mapping images by HAADF and STEM: (a), (c) and (e) corrosion depth, (b), (d) and (f) matrix precipitates and GBPs.

precipitates hinder the movement of dislocations and cause local dislocation entanglement, then the local dislocation density is increased. The partial recrystallized grain structure is finally obtained in the sheets.

The rolling behavior for 7085 alloys can be expressed as that microstructure is considerably changed by large plastic deformation and remnant phases are broken into different sizes which depends on the deformation rate. Also, strong plastic deformation causes high dislocation density, stored energy, and a large volume fraction of the deformed structure. Figure 5a shows plenty of dislocations located along the deformed structures. During heat treatment, static recrystallization gradually occurs as the energy provided by heating is greater than stored energy, but the alloy still maintains certain dislocations, which are displayed in Fig. 5b [25]. The remaining sub-grain indicates that the Al_3Zr precipitate pins the dislocation

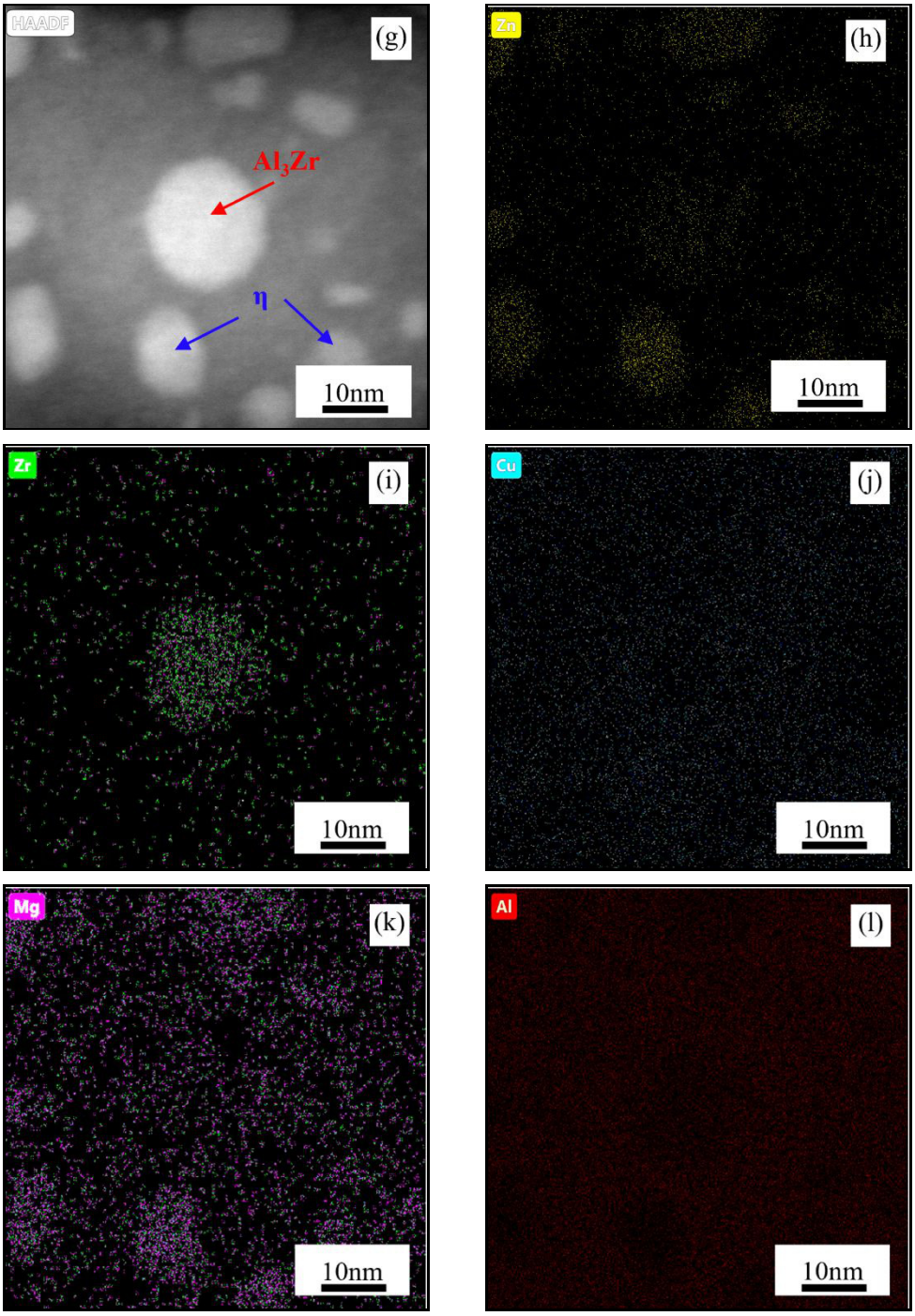

Fig. 7g–l. Corrosion depths and TEM images of precipitate on 1 mm, 2 mm and 3 mm thickness sheets and element mapping images by HAADF and STEM: (g)–(l) mapping images for matrix precipitates.

and prevents LAGBs from effectively absorbing the dislocations in the matrix [26]. Consequently, the partial recrystallized grain and sub-grain coexist in 7085 alloys.

3.3. Surface hardness

A hardness test was performed according to ASTM E18. As shown in Table 2, each average value was

Table 2. Surface hardness from different thickness sheets (HRB)

Thickness (mm)	Test point 1	Test point 2	Test point 3	Ave.
1	87.20	86.50	86.55	86.75
2	86.10	86.30	86.10	86.17
3	84.39	84.89	83.73	84.34

calculated by three values tested on the sheet surface. The result displays that hardness increases with the decrease of thickness and the max. value is 86.75 HRB on the 1 mm sheet in Fig. 6.

The hardness deviation among different thickness sheets is related to the recrystallization rate, dislocation density, and precipitates [3]. Moreover, recrystallization could consume the dislocation density around the sub-grain and decrease hardness [27, 28]. As mentioned in Figs. 2j–l, a low volume fraction of recrystallization in the 1 mm sheet can be concluded, and a high dislocation density tends to concentrate around the sub-grain shown in Fig. 3e and Fig. 4b, respectively.

3.4. IGC performance

The IGC test was conducted based on ASTM G110. Figures 7a,c,e display the corrosion depth on different thickness sheets. The results show that the depth of pitting corrosion develops deeper on thicker sheets and the minimum depth is 9.17 μm on the 1 mm sheet. The corrosion preferentially propagates along the recrystallized grain boundaries shown in Fig. 7e [29]. Figures 6b,d,f exhibit the morphology and distribution of matrix precipitates and GBPs on different thickness sheets. The density of matrix precipitates is not obviously enhanced, while an apparent coarse phenomenon on GBPs appears with the increasing thickness. With the increase in sheet thickness, the width of PFZ gradually decreased from 27.19 to 14.27 nm. The element mapping images by HAADF and STEM in Figs. 7g–l manifest Al_3Zr and η are typical matrix precipitates on Al-Zn-Mg-Cu alloy [17].

The GBPs, PFZ, and recrystallization are mainly considered for the corrosion behavior of different thickness sheets. Generally, the typical IGC mode of 7xxx alloy has been studied, and the anodic dissolution theory is one of the theories to manifest the corrosion mechanism [16, 30]. Two methods can be applied to improve the IGC resistance of 7xxx alloys: one is abating the potential deviation between GBPs and aluminum matrix; the other is decreasing the anodic dissolution rate along the grain boundary [16]. The corrosion behaviors are mainly affected by the morphology of the η phase at grain boundaries in 7xxx alloy. As the negative potential of the η phase compared to the matrix, the η phase as GBPs is preferentially corroded as an anode. Based on the result of this study, the small and discontinuous GBPs help decrease the anodic dissolution rate [21], and the wider PFZ results in a more difficult diffusion of precipitates to form galvanic coupling; therefore, corrosion resistance is improved [31]. In addition, LAGBs usually result from sub-grains for sheet products. Compared with large recrystallized grain, sub-grain shows longer grain boundaries, which decrease the propagation of corrosion channels [32].

It is concluded that inhibition of the recrystallization rate and retaining certain sub-grains are both beneficial for hardness improvement. Discontinuous GBPs, a wider PFZ, and fine sub-grains effectively enhance the intergranular corrosion resistance for 7085 sheets.

4. Conclusions

This work discusses the hot deformation effect on microstructure evolution, hardness, and IGC on different thickness sheets. The main conclusions can be described in the following aspects:

1. The strong plastic deformation changes the remanent phase into small particles. Large plastic deformation contributes to reducing the recrystallization rate and causes texture and dislocation changes after heat treatment.

2. Reducing recrystallization rate and enhancing dislocation density are both favorable to improve hardness for 7085 aluminum alloy sheets when the thickness range is between 1 to 3 mm.

3. Smaller discontinuous GBPs, less recrystallization rate, or increased width of PFZ are beneficial for IGC resistance in the thickness range of 1 to 3 mm.

Acknowledgements

The authors would like to acknowledge the financial support of the Natural Science Foundation of China (Nos. U20A20274, 52071158, 51701085, U1664254), the Six Talents Peak Project of Jiangsu Province (2018-XCL-202), the Open Funds of SKLMMC of SJTU (MMC-KF18-16), the Jiangsu Provincial Key Laboratory of High-end Structural Materials (HSM1803, 1902).

References

[1] P. Dai, X. Luo, Y. Yang, Z. Kou, B. Huang, C. Wang, J. Zang, J. Ru, Nano-scale precipitate evolution and mechanical properties of 7085 aluminum alloy during thermal exposure, Mater. Sci. and Tech. A 729 (2018) 411–422. http://doi.org/10.1016/j.msea.2018.05.092

[2] H. C. Fang, H. Chao, K. H. Chen, Effect of recrystallization on intergranular fracture and corrosion of Al-Zn-Mg-Cu-Zr alloy, J. Alloy Compd. 622 (2015) 166–173. http://doi.org/10.1016/j.jallcom.2014.10.044

[3] J. Liu, P. Yao, N. Zhao, C. Shi, H. Li, X. Li, D. Xi, S. Yang, Effect of minor Sc and Zr on recrystallization behavior and mechanical properties of novel Al-Zn-Mg-Cu alloys, J. Alloy Compd. 657 (2016) 717–725. http://doi.org/10.1016/j.jallcom.2015.10.122

[4] X. Liu, Y. Liu, Z. Zhou, Q. Zhan, Enhanced strength and ductility in Al-Zn-Mg-Cu alloys fabricated by

laser powder bed fusion using a synergistic grain-refining strategy, J. Mater. Sci. Technol. 124 (2022) 41–52. http://doi.org/10.1016/j.jmst.2021.12.078
[5] Y. Bi, Z. Luo, J. Guo, Y. Yang, J. Su, Y. Zhang, Joint formation mechanism and performance of resistance butt spot welding for AA 5754 aluminum alloy sheet, Mater. Lett. 319 (2022) 132279. http://doi.org/10.1016/j.matlet.2022.132279
[6] G. Li, H. Deng, Y. Mao, X. Zhang, J. Cui, Study on AA5182 aluminum sheet formability using combined quasi-static-dynamic tensile processes, J. Mater. Process. Technol. 255 (2018) 373–386. http://doi.org/10.1016/j.jmatprotec.2017.12.038
[7] Z. Xu, S. Luan, S.-Y. Tian, H.-B. Wang, S.-L. Li, L. Zhou, Effect of erbium on microstructure and properties of AA6061 twin-roll casting sheet, J. Alloy Compd. 907 (2022) 164458. http://doi.org/10.1016/j.jallcom.2022.164458
[8] C. Ma, L. Hou, J. Zhang, L. Zhuang, Influence of thickness reduction per pass on strain, microstructures and mechanical properties of 7050 Al alloy sheet processed by asymmetric rolling, Mater. Sci. Eng. A 650 (2016) 454–468. http://doi.org/10.1016/j.msea.2015.10.059
[9] J. Ma, Q. Wang, T. Zhang, H. Cao, Y. Yang, Z. Zhang, Effect of natural aging time on tensile and fatigue anisotropy of extruded 7075 Al alloy, J. Mater. Res. Technol. 18 (2022) 4683–4697. http://doi.org/10.1016/j.jmrt.2022.04.151
[10] G. Xiao, J. Jiang, Y. Liu, Y. Wang, B. Guo, Recrystallization and microstructure evolution of hot extruded 7075 aluminum alloy during semi-solid isothermal treatment, Mater. Charact. 156 (2019) 109874. http://doi.org/10.1016/j.matchar.2019.109874
[11] Z. Gronostajski, K. Jaśkiewicz, P. Kaczyński, M. Skwarski, S. Polak, J. Krawczyk, W. Chorzępa, P. Trzpis, W-Temper forming of B-pillar from 7075 aluminum alloy, CIRP Annals 71 (2022) 221–224. http://doi.org/10.1016/j.cirp.2022.03.019
[12] S. Liu, Q. Li, H. Lin, L. Sun, T. Long, L. Ye, Y. Deng, Effect of quench-induced precipitation on microstructure and mechanical properties of 7085 aluminum alloy, Mater. Des. 132 (2017) 119–128. http://doi.org/10.1016/j.matdes.2017.06.054
[13] Y.-J. Shi, Q.-L. Pan, M.-J. Li, Z.-M. Liu, Z.-Q. Huang, Microstructural evolution during homogenization of DC cast 7085 aluminum alloy, Trans. Nonferrous Met. Soc. China 25 (2015) 3560–3568. http://doi.org/10.1016/s1003-6326(15)63993-0
[14] S. Zhang, X. Luo, G. Y. Zheng, N. Z. Zhai, Y. Q. Yang, P. T. Li, Effect of cryorolling and ageing on the microstructure and mechanical properties of Al 7085 alloy, Mater. Sci. Eng. A 832 (2022)142482. http://doi.org/10.1016/j.msea.2021.142482
[15] J. Liu, Z. Du, J. Su, J. Tang, F. Jiang, D. Fu, J. Teng, H. Zhang, Effect of quenching residual stress on precipitation behaviour of 7085 aluminium alloy, J. Mater. Sci. Technol. 132 (2023) 154–165. http://doi.org/10.1016/j.jmst.2022.06.010
[16] Y. Wang, L. Cao, X. Wu, X. Tong, B. Liao, G. Huang, Z. Wang, Effect of retrogression treatments on microstructure, hardness and corrosion behaviors of aluminum alloy 7085, J. Alloy Compd. 814 (2020) 152264. http://doi.org/10.1016/j.jallcom.2019.152264
[17] Y. Zou, L. Cao, X. Wu, Y. Wang, X. Sun, H. Song, M. J. Couper, Effect of ageing temperature on microstructure, mechanical property and corrosion behavior of aluminum alloy 7085, J. Alloy Compd. 823 (2020) 153792. http://doi.org/10.1016/j.jallcom.2020.153792
[18] H. Zhu, P. Ma, C. Liu, J. He, J. Yang, L. Chen, L. Huang, L. Zhan, Effect of cryogenic pre-deformation on the stress relaxation response and mechanical/corrosion properties in Al-Zn-Mg-Cu alloy, J. Mater. Res. Technol. 20 (2022) 3471–3484. http://doi.org/10.1016/j.jmrt.2022.08.084
[19] Q. Cheng, L. Ye, Q. Huang, Y. Dong, S. Liu, Effect of two-stage overaging on microstructure and corrosion properties of an Al-Zn-Mg-Cu alloy, J. Mater. Res. Technol. 20 (2022) 3185–3194. http://doi.org/10.1016/j.jmrt.2022.08.098
[20] H. Zhong, S. Li, Z. Zhang, D. Li, H. Deng, J. Chen, L. Qi, O. A. Ojo, Precipitation behavior, mechanical properties, and corrosion resistance of rare earth-modified Al-Zn-Mg-Cu alloys, Mater. Today Commun. 31 (2022) 103732. http://dx.doi.org/10.1016/j.mtcomm.2022.103732
[21] Y. Pan, D. Zhang, H. Liu, L. Zhuang, J. Zhang, Precipitation hardening and intergranular corrosion behavior of novel Al-Mg-Zn(-Cu) alloys, J. Alloy Compd. 853 (2021) 157199. http://doi.org/10.1016/j.jallcom.2020.157199
[22] H. Xiao, Z. Wang, J. Geng, C. Zhang, Y. Li, Q. Yang, M. Wang, D. Chen, Z. Li, H. Wang, Precipitation and crystallographic relationships of nano-sized η/η' precipitates at S-Al interface in Al-Zn-Mg-Cu alloy, Scripta Mater. 214 (2022) 114643. http://doi.org/10.1016/j.scriptamat.2022.114643
[23] L. Jiang, Z. Zhang, H. Fu, S. Huang, D. Zhuang, J. Xie, Corrosion behavior and mechanism of Al-Zn-Mg-Cu alloy based on the characterization of the secondary phases, Mater. Charact. 189 (2022) 111974. http://dx.doi.org/10.1016/j.matchar.2022.111974
[24] C. Xu, J. Huang, F. Jiang, Y. Jiang, Dynamic recrystallization and precipitation behavior of a novel Sc, Zr alloyed Al-Zn-Mg-Cu alloy during hot deformation, Mater. Charact. 183 (2022) 111629. http://dx.doi.org/10.1016/j.matchar.2021.111629
[25] H. C. Fang, F. H. Luo, K. H. Chen, Effect of intermetallic phases and recrystallization on the corrosion and fracture behavior of an Al-Zn-Mg-Cu-Zr-Yb-Cr alloy, Mater. Sci. Eng. A 684 (2017) 480–490. http://doi.org/10.1016/j.msea.2016.12.009
[26] J.-F. Leng, B.-H. Ren, Q.-B. Zhou, J.-W. Zhao, Effect of Sc and Zr on recrystallization behavior of 7075 aluminum alloy, Trans. Nonferrous Met. Soc. China 31 (2021) 2545–2557. http://doi.org/10.1016/s1003-6326(21)65674-1
[27] Y. Zhang, J. Jiang, Y. Wang, G. Xiao, Y. Liu, M. Huang, Recrystallization process of hot-extruded 6A02 aluminum alloy in solid and semi-solid temperature ranges, J. Alloy Compd. 893 (2022) 162311. http://doi.org/10.1016/j.jallcom.2021.162311
[28] X. W. Yu, J. H. Chen, J. Y. Li, C. L. Wu, X. B. Yang, Effect of pre-deformation on quench-induced inhomogeneity of microstructure and hardness in 7050 aluminum alloy, Mater. Charact. 158 (2019) 110005.

http://doi.org/10.1016/j.matchar.2019.110005
[29] Y. Li, B. Lu, W. Yu, J. Fu, G. Xu, Z. Wang, Two-stage homogenization of Al-Zn-Mg-Cu-Zr alloy processed by twin-roll casting to improve L12 Al3Zr precipitation, recrystallization resistance, and performance, J. Alloy Compd. 882 (2021) 160789. http://doi.org/10.1016/j.jallcom.2021.160789
[30] X. Peng, Q. Guo, X. Liang, Y. Deng, Y. Gu, G. Xu, Z. Yin, Mechanical properties, corrosion behavior and microstructures of a non-isothermal ageing treated Al-Zn-Mg-Cu alloy, Mater. Sci. Eng. A 688 (2017) 146–154. http://doi.org/10.1016/j.msea.2017.01.086
[31] J. Li, F. Li, X. Ma, J. Li, S. Liang, Effect of grain boundary characteristic on intergranular corrosion and mechanical properties of severely sheared Al-Zn-Mg-Cu alloy, Mater. Sci. Eng. A 732 (2018) 53–62. http://doi.org/10.1016/j.msea.2018.06.097
[32] A. Lervik, S. Wenner, O. Lunder, C. D. Marioara, R. Holmestad, Grain boundary structures and their correlation with intergranular corrosion in an extruded Al-Mg-Si-Cu alloy, Mater. Charact. 170 (2020) 110695. http://doi.org/10.1016/j.matchar.2020.110695